energies

MDPI

Article

Theoretical Investigations of the $BaRh_2Ge_4X_6$ (X = S, Se, Te) Compounds

Pascal Boulet [1,*] and Marie-Christine Record [2]

[1] Aix-Marseille University, UFR Sciences, CNRS, Madirel, 13013 Marseille, France
[2] Aix-Marseille University, UFR Sciences, CNRS, IM2NP, 13013 Marseille, France; m-c.record@univ-amu.fr
* Correspondence: pascal.boulet@univ-amu.fr

Received: 29 October 2020; Accepted: 2 December 2020; Published: 5 December 2020

Abstract: The thermoelectric (TE) properties of the $BaM_2Ge_4X_6$ compounds, where M = Rh and X = S, Se, Te, were investigated by computational approaches using density-functional theory and semi-classical Boltzmann theory for electronic transport. It was found that these compounds bear good TE properties, in particular $BaRh_2Ge_4Te_6$, for which the figure of merit was estimated to reach 1.51 at 300 K. As this compound has not yet been proved to be stable, we also investigated $BaRh_2Ge_4S_4Te_2$ by assuming that replacing tellurium by sulphur could stabilize the tellurium-containing structure. It was found that the TE properties are good. The quantum theory of atoms in molecules was used to investigate the nature of the chemical interactions that prevail in these compounds. A wide variety of interactions were evidenced, from van der Waals interactions to ionic and polar-covalent ones, which could explain the good TE performance of these compounds.

Keywords: thermoelectricity; chalcogenides; DFT calculations; transport properties; QTAIM

1. Introduction

Research for new materials with specific properties is currently very active in the field of energy. Rationalization of material design is a key in the development of new materials, albeit the most difficult to achieve. This is particularly relevant in the field of thermoelectricity in which good materials should exhibit mutually counteracting properties. Indeed, the thermoelectric (TE) performance is measured by the figure of merit $ZT = \alpha^2\sigma T/\kappa$, where α, σ and κ are the Seebeck coefficient, the electrical conductivity and the thermal conductivity, respectively, for which the electrical conductivity is inversely and directly related to the Seebeck coefficient and the thermal conductivity, respectively. In effect, as both electronic and phononic contributions come into play in thermal conductivity, high electron and phonon thermal transport undermines ZT. Many strategies, such as nanostructuring [1–3] and rattlers insertion in structure cavities [4–7], have demonstrated a certain success in reducing the thermal conductivity, while not affecting the electrical one, by reducing the lattice contribution part. Another strategy is based on the bands or orbital engineering related to the manipulation of orbital energies to achieve degenerated electronic states near the Fermi level—e.g., either by searching for low crystal field splitting energy compounds [8] or resonant levels [9] or by applying strains on the structures [8,10,11]. This type of approach, based on the fact that electronic characteristics govern the material properties at the very microscopic scale, allows us to infer that a description of the structure–property relationship can be described using the bonding features of the materials. This indeed has shown to be successful in the realm of molecular systems with the development of global and local reactivity indices (see for instance [12–18] and references therein). The quantum theory of atoms in molecules (QTAIM) [19] and its extension to crystals QTAIMAC [20] also provide a solid quantum-based background for rationalizing and quantifying structure–property relationships in molecules and crystals.

Recently, 2D van der Waals materials have been shown to exhibit good thermoelectric properties owing to their specific structure that can enhance the electrical conductivity and lower the thermal one [21–23]. In a recent work, a series of new, layered compounds was discovered [24] that presents a variety of chemical bonding types. These compounds with general formula $BaM_2Ge_4X_6$, where M is a transition metal atom of group 9 (Rh, Ir) and X a chalcogenide atom (S, Se), could present good thermoelectric properties owing to the layered structure and wide spectrum of different atom masses, which could lead to low thermal conductivity. Therefore, the purpose of this work is to investigate the TE properties of these compounds and use QTAIMAC as a tool to shed light on their structure–property relationships.

2. Bader's Quantum Theory of Atoms in Molecules and Computational Details

2.1. Bader's Quantum Theory of Atoms in Molecules

We give in this section a brief, partial account of Bader's QTAIMAC for the purpose of our work.

The quantum theory of atoms in molecules and crystals (QTAIMAC) developed by R.W. Bader is a powerful theory that allows for analysing the nature of chemical bonds from the topology of the electron density [20,25]. The analysis is based on the electron density $\rho(r)$ and its successive spatial derivatives, namely the gradient field $\nabla\rho(r)$ and the Laplacian $\nabla^2\rho(r)$. The atomic nuclei, where the electron density reaches a maximum, are termed attractors. Starting from the attractors, the electron density decreases continuously until the gradient vector field zeroes out, hence defining a limiting volume of the atom called the atomic basin. Special attention must be paid to the so-called bond path, which should, however, not be confused with the restricted notion of chemical bond [26]. The bond path is a line that joins two nuclei where the electron density is a maximum in the direction of the path and a minimum in the two perpendicular directions. Starting from both attractors, the lines connect at the boundary of the atomic basins, where the gradient vanishes, at a point named the bond critical point. Hence, two atoms are said to be bonded when they are connected through a bond path and a bond critical point (BCP). The BCP resides at the minimum of the bond path and is characterized by the signature (3, −1). The signature is a property of critical points granted by the electron density Laplacian and noted (ω, σ), where ω is the rank of the Laplacian matrix and σ is the algebraic sum of the Laplacian eigenvalues signs. From this definition, there exists four types of critical points in solids: the attractor with signature (3, −3), the BCP with signature (3, −1), the ring critical points (RCP) with signature (3, 1) and the cage critical point (CCP) with signature (3, 3). For BCPs, the Laplacian eigenvalues are ranked as $\lambda_1 \leq \lambda_2 \leq 0 \leq \lambda_3$ and denote an incoming flow of electron density perpendicular to the bond path (λ_1 and λ_2) and an escaping flow of electron density parallel to the bond path (λ_3). Many property indices have been derived from the properties of the Laplacian such as the ellipticity [20], the metallicity [20,27,28] or the polarity [29] of a bond, to cite a few, and the various kinds of chemical bonding have been characterized (shared-shell, closed-shell, polar covalent, etc.; see for instance [20] and references therein) based on these properties. An important relation has been derived [19] that relates the kinetic $G(r)$ and potential $V(r)$ energy densities to the electron density Laplacian. Indeed, $\nabla^2\rho(r)$ appears in the local expression of the Virial theorem as:

$$1/4\,\nabla^2\rho(r) \;=\; 2G(r) \;+\; V(r) \tag{1}$$

As a consequence, the sign of the Laplacian expresses the relative dominance of the kinetic or potential energy density at any point r in space, in particular at the BCP location from which we can then draw conclusions on the nature of the chemical bonding. There remains to evaluate the kinetic and potential energy densities. In the following, we used for $G(r)$ a model derived from the Thomas-Fermi expression of the kinetic energy density that was further refined by Kirzhnits [30] (see also [31]) and Abramov [32]:

$$G(r) = \frac{3}{10}\left(3\pi^2\right)^{\frac{2}{3}}\rho(r)^{\frac{5}{3}} + \frac{1}{72}\frac{[\nabla\rho(r)]^2}{\rho(r)} + \frac{1}{6}\nabla^2\rho(r) \tag{2}$$

The potential $V(r)$ can then be obtained from Equation (1) knowing the Laplacian.

2.2. Computational Details

Density-functional theory calculations [33,34] were carried out at the generalized gradient approximation employing the PBE [35] exchange-correlation functional and projected-augmented planewaves [36] as pseudopotentials (PSP). Semi-core states were accounted for in the valence shells of most of the atoms and that separate core electrons from valence ones. The valence configuration of the atoms are as follows: Ba: $5s^2 5p^6 6s^2$; Rh: $4s^2 4p^6 5s^2 4d^7$; Ge: $4s^2 3d^{10} 4p^6$; S, Se: $ns^2 np^4$ (n = 2, 3); Te: $5s^2 4d^{10} 5p^4$. The structures were optimized until the following thresholds were met: 10^{-7} Ry for the energy, 0.1 mRy bohr^{-1} for the forces, 10^{-10} for the wavefunction coefficients and 0.01 kbar for the cell. The energy and electron density cutoffs were set to 45 Ry and 450 Ry, respectively. The Monkhorst-Pack scheme was used to set up the k-point grid. For structure optimizations, the grid contained 72 k-points, whereas 576 k-points were used for band structures, projected density of states and thermoelectric-related calculations. Both full relativistic (including spin-orbit coupling) and non-relativistic calculations were performed. Our choice for the PBE functional is based on the following observations: (i) the PBE yields good optimized structures (cell parameters and atomic positions) compared with experimental data and satisfactory chemical and physical properties, whereas the PBEsol functional sometimes yields better structural parameters [37] but often worse properties [38]. (ii) With hybrid functionals, the band structure should be comparable to that of PBE [39]. The electronic gap of the compounds should be larger than with PBE [39], but it is not 100% guaranteed. If we could assume that with hybrid functionals, the d electrons are better localized and thus the material properties better reproduced, this is not always the case [40]. Moreover, the corresponding calculations with hybrid functionals are far more computationally expensive.

The thermoelectric properties were determined as follows. The DFT-calculated bands are extrapolated using a smoothed Fourier expansion. Using the constant relaxation time approximation, the electrical conductivity and Seebeck coefficient can then be calculated according the following set of equations:

$$\sigma_{\alpha\beta}(T,\mu) = \frac{1}{\Omega}\int \sigma_{\alpha\beta}(i,k)\left(-\frac{\partial f_\mu(T,\epsilon)}{\partial \epsilon}\right) \tag{3}$$

where Ω is the unit cell volume, $f_\mu(T,\epsilon)$ is the Fermi-Dirac distribution, μ is the electron chemical potential, T is the temperature, ϵ is the electronic energy states and $\sigma_{\alpha\beta}(i,k)$ is the electrical conductivity tensor for a given state i at k-point k.

$$\sigma_{\alpha\beta}(i,k) = e^2 \tau_{i,k} v_\alpha(i,k) v_\beta(i,k) \tag{4}$$

where $v_\alpha(i,k)$ is the group velocity in the α direction such that:

$$v_\alpha(i,k) = \frac{1}{\hbar} \times \frac{\partial \epsilon_{i,k}}{\partial k_\alpha} \tag{5}$$

From the definition of the transport function:

$$\nu_{\alpha\beta}(T,\mu) = \frac{1}{eT\Omega}\int \sigma_{\alpha\beta}(i,k)\left(-\frac{\partial f_\mu(T,\epsilon)}{\partial \epsilon}\right) \tag{6}$$

The Seebeck coefficient tensor reads:

$$S_{\gamma\eta}(T,\mu) = \frac{\nu_{\alpha\eta}(T,\mu)}{\sigma_{\alpha\gamma}(T,\mu)} \tag{7}$$

The power factor was calculated as the product $PF = S^2\sigma$.

The quantum Espresso 6.2 package was used for DFT calculations [41,42]. For electronic transport calculations, the BoltzTraP program [43] was used. The topological properties of the electron density were calculated with the Critic2 program [44,45]. The structures visualization was performed with VESTA 3.5.2 [46], and the valence-shell charge concentration and energy densities were plotted with gnuplot 5.2 [47].

3. Structural, Electronic and Transport Results

In this section, the results for the $BaRh_2Ge_4X_6$ (X = S, Se) compounds as well as the hypothetical $BaRh_2Ge_4Te_6$ one are presented in the first part. The results obtained for the $BaRh_2Ge_4S_4Te_2$ hypothetical structure are the subject of the second part.

3.1. $BaRh_2Ge_4X_6$ (X = S, Se, Te)

3.1.1. Structural Characteristics of the Compounds

The $BaRh_2Ge_4X_6$ (X = S, Se) are known to crystallize in the orthorhombic, Pbca crystallographic group [25]. The corresponding Bravais lattice is the face-centred orthorhombic one. Hence, all the structures were optimized in this system, including the hypothetical $BaRh_2Ge_4Te_6$ one. The corresponding parameters are given in Table 1. The predicted parameters are slightly larger than the experimental ones, and the deviations range from 0.84% to 1.42%. As expected, the parameters increase from sulphur-to selenium-and tellurium-containing compounds. The $BaRh_2Ge_4X_6$ (X = S, Se, Te) structures are depicted in Figure 1. The barium atom is surrounded by six chalcogen atoms forming a nearly regular dodecahedron picture. These dodecahedra are connected to each other by sharing faces and pave the ab plane. Two types of chalcogen atoms, named X2 and X3 in the crystallographic database, are bonded to the barium atoms. The X3 chalcogen atoms are capped above four barium atoms and bonded to a germanium one, exhibiting a distorted squared pyramid. The X2 chalcogen atoms are bonded to one barium atom and three germanium ones, forming a distorted tetrahedron. The rhodium atoms are at the centre of a distorted squared bipyramid for which the vertices are constituted by three chalcogen of type X1 and three germanium atoms. These bipyramids are slightly slanted with respect to the c crystallographic axis by 17.3° for $BaRh_2Ge_4S_6$, 18.6° for $BaRh_2Ge_4Se_6$ and 20.7° for $BaRh_2Ge_4Te_6$. The bipyramids are connected to one another by corners being either germanium or a chalcogen and form a double-layer enclosed between the dodecahedra and expanding along the ab plane. These structures can hence be categorized as layered ones.

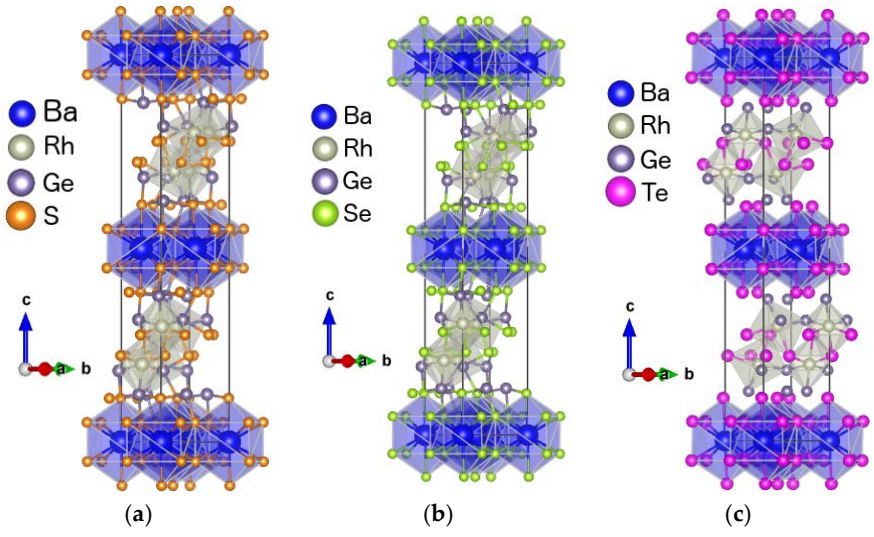

Figure 1. Structures of the $BaRh_2Ge_4S_6$ (**a**), $BaRh_2Ge_4Se_6$ (**b**) and $BaRh_2Ge_4Te_6$ (**c**) compounds. Barium atoms are big balls in blue, rhodium in grey, germanium in purple, sulphur in orange, selenium atoms are small balls in green and Te in magenta.

Table 1. Optimized crystallographic parameters of the $BaRh_2Ge_4X_6$ (X = S, Se, Te) structures (experimental parameters in parenthesis from [25]).

Parameter (Å)	$BaRh_2Ge_4S_6$	$BaRh_2Ge_4Se_6$	$BaRh_2Ge_4Te_6$
a	6.022 (5.9473(2))	6.219 (6.1318(3))	6.506
b	5.967 (5.8891(2))	6.156 (6.0700(3))	6.458
c	29.424 (29.1781(9))	30.626 (30.3144(9))	32.580

3.1.2. Electronic Structures

The possible existence of magnetism was investigated for these structures. Assuming that magnetism could arise from the electron spin polarization in the rhodium atoms, non-relativistic ferromagnetic calculations were undertaken that converge towards a non-magnetic state. Therefore, it is assumed that these structures do not exhibit magnetism. The band structures of the $BaRh_2Ge_4X_6$ compounds are depicted in Figure 2. Both full-relativistic (FR) and non-relativistic (NR) calculations are superimposed for comparison.

There are few differences between the FR and NR results. The energy gaps are about the same, except for the Te-containing compound. The corresponding data are gathered in Table 2. The band gaps are indirect ones for $BaRh_2Ge_4Se_6$ and $BaRh_2Ge_4Te_6$, and direct for $BaRh_2Ge_4S_6$. The gap energy decreases from sulphur to selenium and to tellurium from 1.27 to 1.0 and 0.35 eV; thus, these compounds are semi-conductors with a medium to small size band gap. For both $BaRh_2Ge_4Se_6$ and $BaRh_2Ge_4Te_6$, the edge valence state is fairly flat around the Γ k-point along the symmetry lines $X \rightarrow \Gamma \rightarrow Y$. We can note the symmetrical evolution of the edge valence state of $BaRh_2Ge_4Te_6$ along these symmetry lines leading to two equally high-energy points for the valence band. In addition, for this compound, the FR conduction band is downshifted with respect to the NR one, which leads to a smaller FR energy gap.

Table 2. Electronic band characteristics of the $BaRh_2Ge_4X_6$ compounds. NR: non-relativistic; FR: full-relativistic. Gap energies in eV.

	Gap Energy	Band Gap Type	Edge Valence State Features	Edge Conduction State Features
		$BaRh_2Ge_4S_6$		
NR	1.26	Direct, $S-X \rightarrow S-X$	Ge-p, S-p	Rh-d, Ge-s, S-p
FR	1.27	Direct, $S-X \rightarrow S-X$	–	–
		$BaRh_2Ge_4Se_6$		
NR	1.01	Indirect, $\Gamma \rightarrow S-X$	Ge-p, Se-p	Rh-d, Ge-s, Se-p
FR	1.00	Indirect, $\Gamma \rightarrow S-X$	–	–
		$BaRh_2Ge_4Te_6$		
NR	0.48	Indirect, $\Gamma-X/\Gamma-Y \rightarrow S-X$	Ba-d, Ge-p, Te-p	Rh-d, Ge-s, Te-p
FR	0.35	Indirect, $\Gamma-X/\Gamma-Y \rightarrow S-X$	–	–

The density of states (DOS) was projected onto the atomic orbitals. The total DOS and its projections are depicted in Figure 3, and the main atomic contributions to the highest occupied and lowest vacant states are given in Table 2. These contributions are basically the same for all the three compounds. The edge valence state is mainly composed of the germanium and sulphur p orbitals, whereas the edge conduction state is mainly composed of the rhodium d, germanium s and sulphur p orbitals.

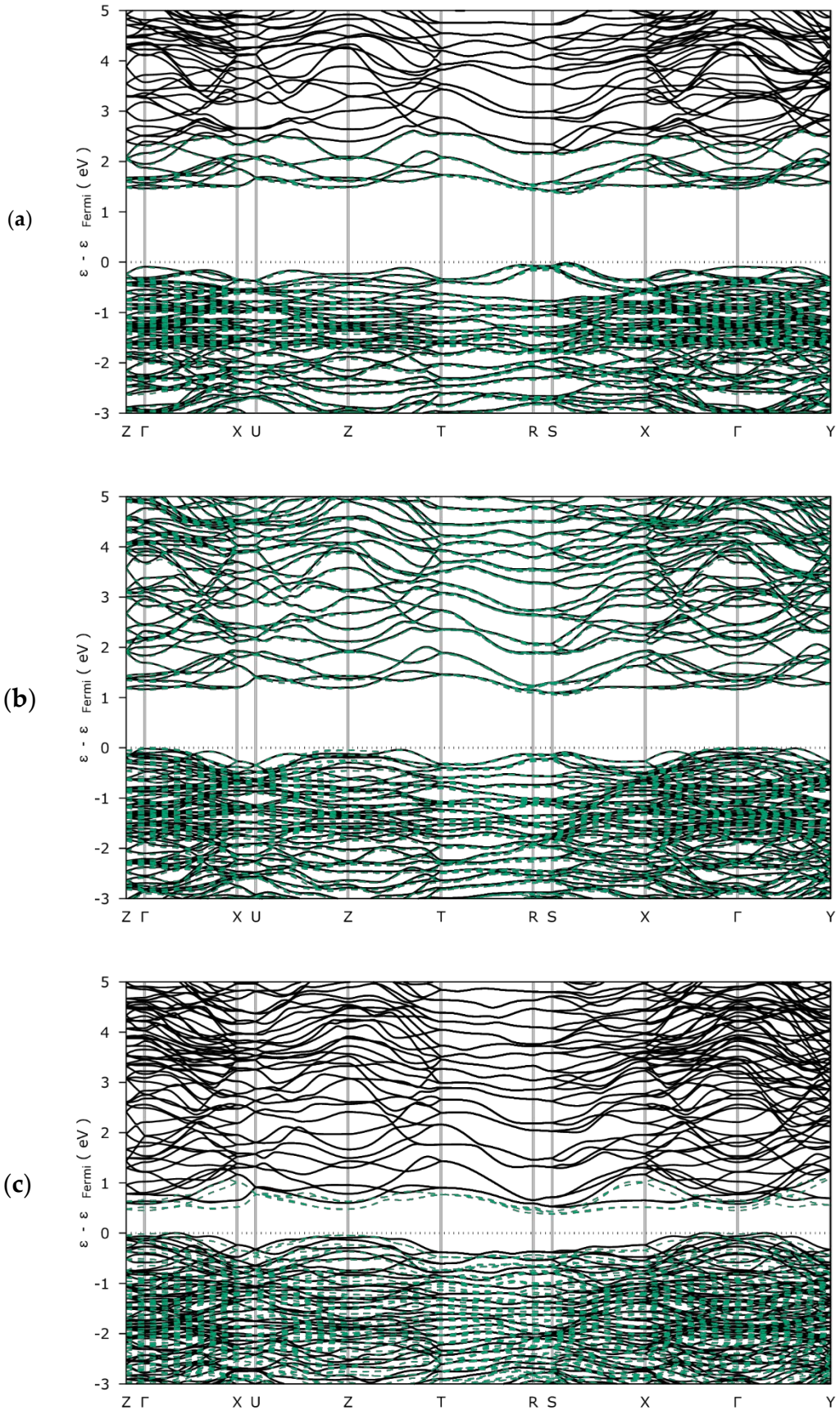

Figure 2. Relativistic (green) and non-relativistic (black) electronic band structures. (**a**) $BaRh_2Ge_4S_6$; (**b**) $BaRh_2Ge_4Se_6$; (**c**) $BaRh_2Ge_4Te_6$.

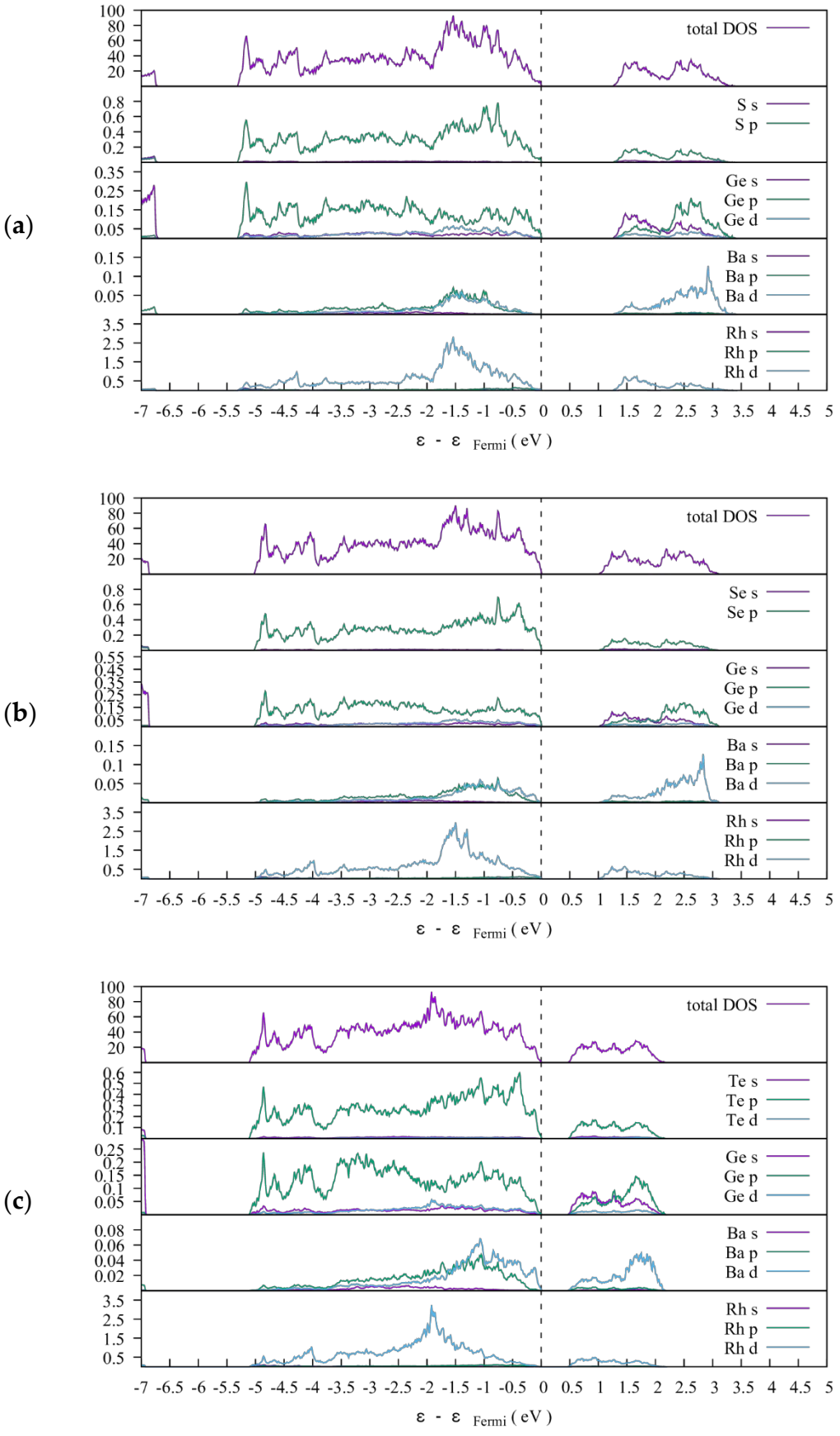

Figure 3. Total and atomic orbital-projected density of states (DOS). (**a**) $BaRh_2Ge_4S_6$; (**b**) $BaRh_2Ge_4Se_6$; (**c**) $BaRh_2Ge_4Te_6$. The projected DOS are scaled by the number of corresponding atoms.

3.1.3. Thermoelectric Properties

We focused on the electronic part of the thermoelectric properties, namely the Seebeck coefficient S, the electrical conductivity σ and the power factor $S^2\sigma$. Since the size of the structures is large, the calculation of the thermal conductivity is not tractable. The TE properties are presented in Figure 4. Regarding the Seebeck coefficient, it decreases as the temperature increases and along the series S, Se, Te. The maximum peak is located within the limit of 5 k_BT, hence the material properties could be improved by appropriate doping. From the S, to Se and to Te-containing compounds the Seebeck coefficient at 300 K evolves from the extremely high value of 2000 $\mu V/K$ down to 550 $\mu V/K$. These large values are caused by two factors, namely the rather large electronic gap, especially for $BaRh_2Ge_4S_6$, and the decent DOS amplitude near the Fermi level, due to the Ge-p and S/Se/Te-p orbitals, which results from the relatively flat crystal orbitals near the valence and conduction band edges. The Seebeck coefficient falls rapidly as the temperature rises. At 600 K, S amounts to 1000 , 820 and 270 $\mu V/K$ for $BaRh_2Ge_4S_6$, $BaRh_2Ge_4Se_6$ and $BaRh_2Ge_4Te_6$, respectively. The relatively low electrical conductivities contrast with the high Seebeck coefficients. At 300 K, the electrical conductivities scaled by the electrons relaxation time corresponding to the maximum Seebeck coefficient amount to around 2.81×10^9, 1.22×10^{11} and 1.67×10^{16} $\Omega^{-1}m^{-1}s^{-1}$, for the three compounds. Considering an average estimate of 10^{-12} s for the electrons relaxation time τ, the electrical conductivities are about 2.81, 12.2 and 16,700 $\Omega^{-1}m^{-1}$ for the S-, Se-and Te-containing compounds, respectively. The aforementioned assets for the Seebeck coefficients, particularly the large electronic gap, are now detrimental to the electrical conductivities. Nonetheless, decent values of the power factors (scaled by τ and for the largest S value) for the three compounds are obtained at 600 K: 0.437, 2.25 and 50 $mWm^{-1}s^{-1}$. In spite of the lack of available thermal conductivity κ values for these compounds, the figures of merit were estimated from the calculated power factor values using an ad hoc value for κ. It has been shown in literature that in complex structures containing many different atoms with very different masses, bearing large crystallographic unit cell, such as argyrodite [48] or $BaAg_2SnSe_4$ [49], the lattice thermal conductivity can be as low as 0.26 $Wm^{-1}K^{-1}$. Thus, we considered a conservative thermal conductivity for this type of compound to amount to 1 $Wm^{-1}K^{-1}$. The results are depicted in Figure 5. One can observe that the figure of merit increases sharply with the temperature. The largest ZT value was obtained for $BaRh_2Ge_4Te_6$ (1.51 at 300 K), which can be explained both by the small electronic gap that implies a large electrical conductivity and the decent Seebeck coefficient value. For $BaRh_2Ge_4S_6$ and $BaRh_2Ge_4Se_6$, the corresponding values are extremely small and amount to 3.37×10^{-6} and 1.01×10^{-4}, respectively. Larger values were obtained at 600 K (0.26 and 1.35). At high temperatures, the ZT values are probably overestimated due to the accumulated approximations on the electron relaxation time and thermal conductivity values, which vary with the temperature and the electronic band energies.

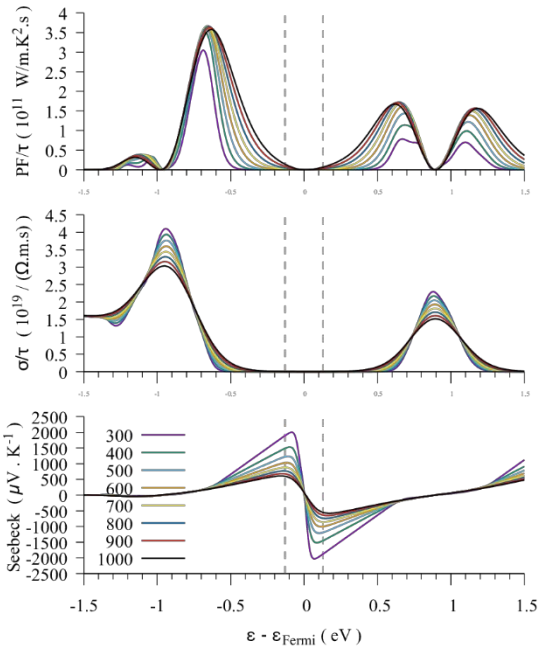

(**a**)

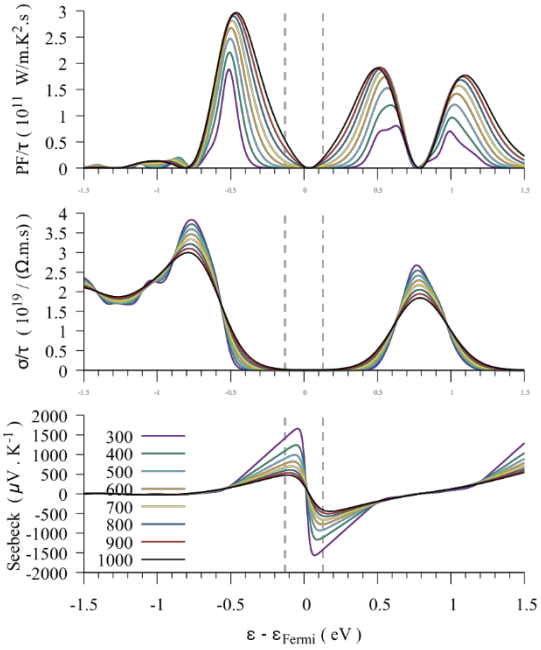

(**b**)

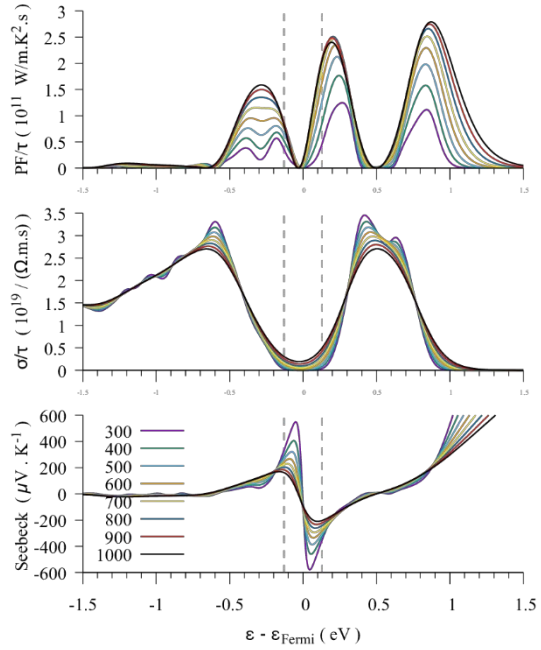

(**c**)

Figure 4. Thermoelectric properties of (**a**) $BaRh_2Ge_4S_6$, (**b**) $BaRh_2Ge_4Se_6$ and (**c**) $BaRh_2Ge_4Te_6$, from 300 to 1000 K. Bottom: Seebeck coefficient; middle: electrical conductivity; top: power factor. The dashed vertical lines delineate the energy 5 k_BT around the Fermi level.

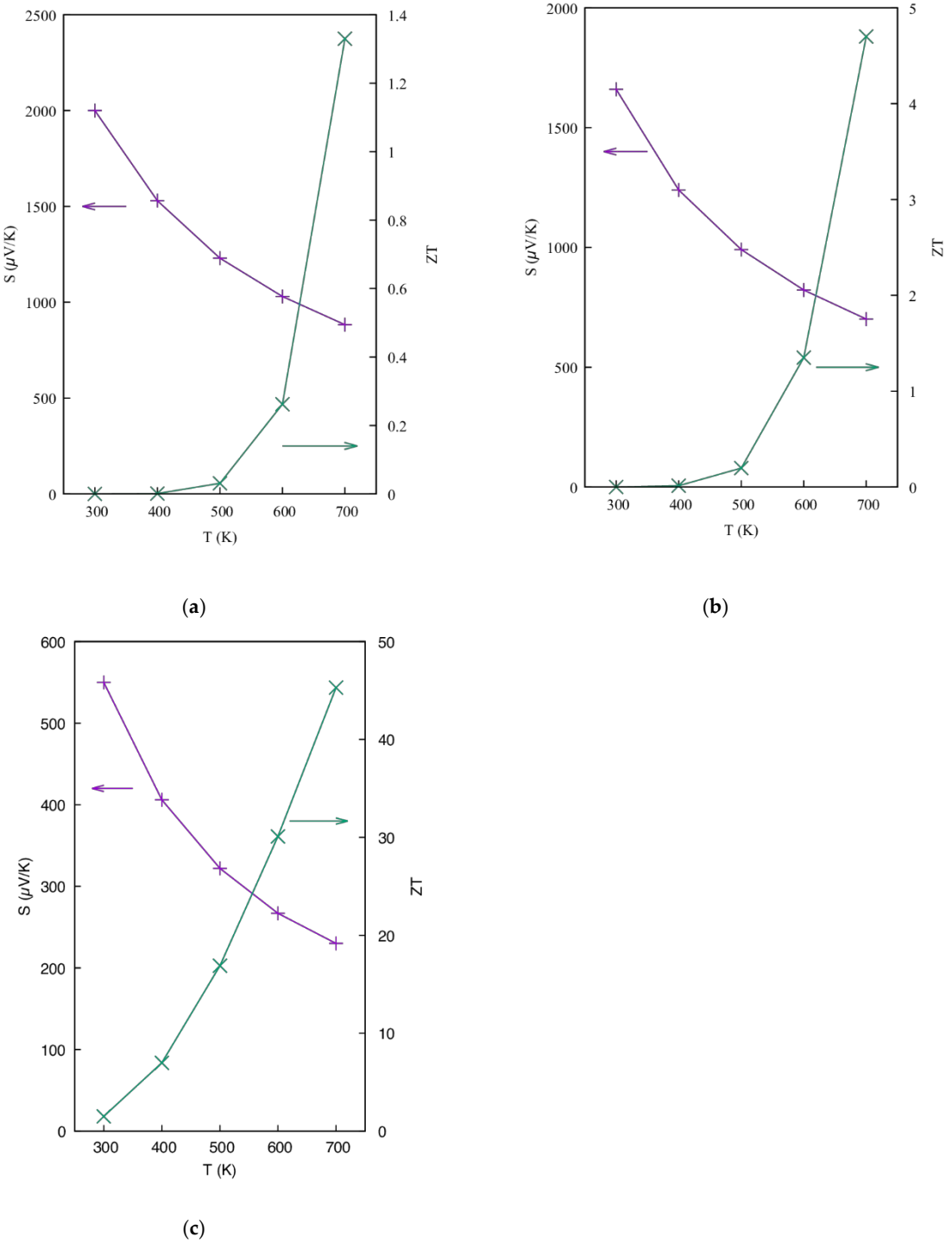

Figure 5. Maximum Seebeck S coefficient and figure of merit *ZT* with respect to temperature. (**a**) $BaRh_2Ge_4S_6$; (**b**) $BaRh_2Ge_4Se_6$; (**c**) $BaRh_2Ge_4Te_6$.

3.2. The $BaRh_2Ge_4S_4Te_2$ Compound

Since Lei et al. reported that neither $BaIr_2Ge_4Te_6$ nor $BaRh_2Ge_4Te_6$ form [24], we investigated $BaRh_2Ge_4S_4Te_2$ by assuming that replacing tellurium by sulphur could stabilize the tellurium-containing structure. Indeed, the mixing energy related to the formation of $BaRh_2Ge_4S_4Te_2$ from $BaRh_2Ge_4Te_6$ and $BaRh_2Ge_4S_6$ is relatively negative (-105.7 kJ.mol^{-1}). In addition, the combination of sulphur and tellurium offers the advantage of obtaining good TE properties due to the presence of tellurium and of lowering the compound risk due to the presence of sulphur. Hence, we calculated the electronic and TE properties of this, yet to be synthesized, compound. The tellurium atoms were placed on the 8c Wyckoff positions, same as for sulphur, connected to the Rh atoms and forming one of the octahedron faces. In $BaRh_2Ge_4X_6$ (X = S, Se), the chalcogen atoms are all located on the 8c Wyckoff positions with free coordinates (x,y,z). Hence, one out of the three sulphur positions was populated with Te atoms, which represents 25.1 wt.% or 15.4 at.% (for comparison, for sulphur the amount is 12.6 wt.% or 30.8 at.%). The optimized crystal structure of $BaRh_2Ge_4S_4Te_2$ is very similar to that of the single-type chalcogen compounds (Figure 6). The cell parameters are $6.294 \times 6.239 \times 29.948$ Å, the a and b parameters being close to those of $BaRh_2Ge_4Se_6$ and c being about midway between those of $BaRh_2Ge_4S_6$ and $BaRh_2Ge_4Se_6$.

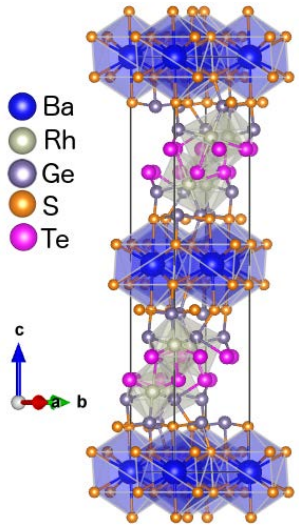

Figure 6. Crystal structure of $BaRh_2Ge_4S_4Te_2$. Barium atoms are big balls in blue, rhodium in grey, germanium in purple, sulphur in orange, selenium atoms are small balls in green, Te in magenta.

The mixture of S and Te in the structure leads to a markedly different electronic band structure as can be seen in Figure 7. First, the bands are not as flat near the band edges as those of the single-type chalcogen compounds. Next, the valence band maximum (VBM) and the conduction band minimum (CBM) are shifted with respect to those of the previous compounds. The VBM is indistinguishably located between the $Z \rightarrow T$ and $\Gamma \rightarrow Y$ symmetry lines and the CBM expands along the $\Gamma \rightarrow Z$ line. Hence, the electronic gap is indirect and is estimated to be 0.71 eV. This value is intermediate between that of $BaRh_2Ge_4Se_6$ and that of $BaRh_2Ge_4Te_6$. As with the previous compounds, the relativistic effects are negligible. The orbital-projected DOS show that the main contributions near the Fermi level arise from the *p* orbitals of the chalcogen atoms and from the germanium ones (Figure 8). It is noticeable that the Te contribution is particularly important compared to that of sulphur.

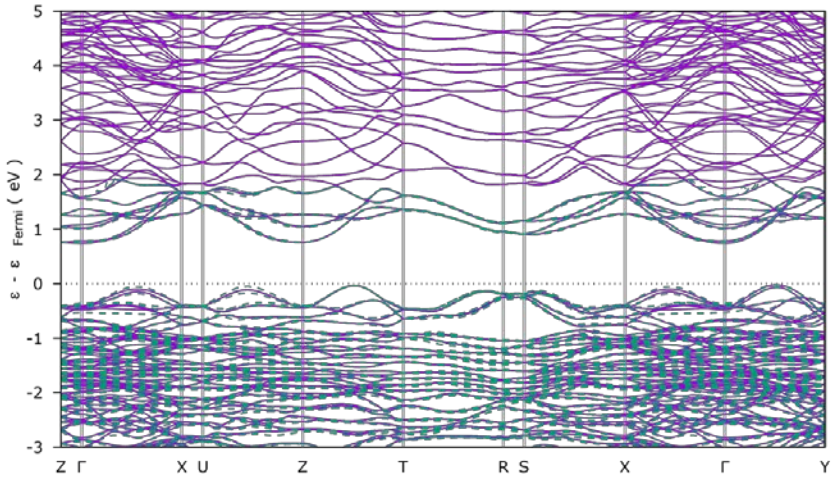

Figure 7. Relativistic (green) and non-relativistic (purple) electronic band structures of $BaRh_2Ge_4S_4Te_2$.

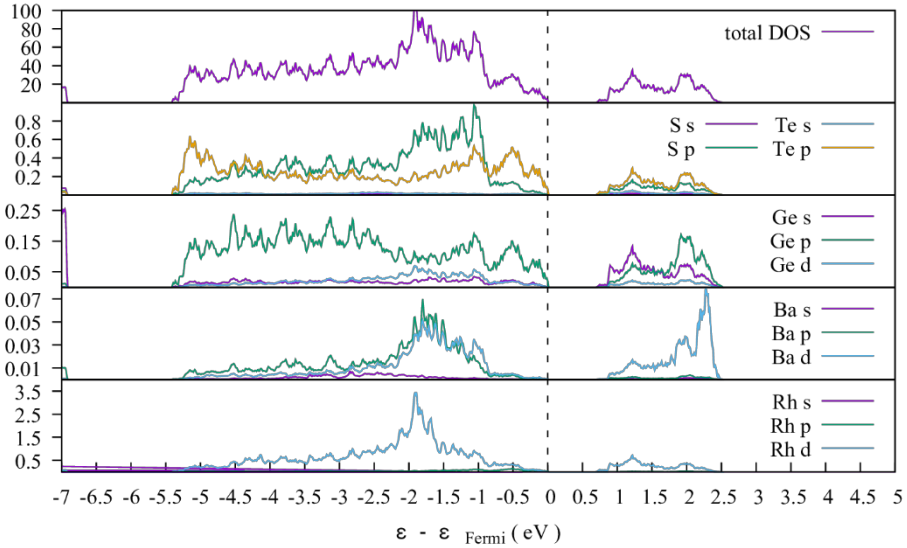

Figure 8. Total and atomic orbital-projected density of states (DOS) of $BaRh_2Ge_4S_4Te_2$. The projected DOS are scaled by the number of corresponding atoms.

The thermoelectric properties of $BaRh_2Ge_4S_4Te_2$ are depicted in Figure 9. The maximum Seebeck coefficient amounts to 1160 µV/K at 300 K and decreases down to about 570 µV/K at 600 K. These values are intermediate between those of $BaRh_2Ge_4Se_6$ and $BaRh_2Ge_4Te_6$. By contrast to the single chalcogen containing compounds, since the orbitals of $BaRh_2Ge_4S_4Te_2$ are not particularly flat near the band edges, this may not be the most important reason for the large Seebeck coefficient. The electronic gap of the compound is a plausible explanation. At the maximum Seebeck coefficient, the electrical conductivity amounts to 44.6 $\Omega^{-1}m^{-1}$ at 300 K, rising to 82,800 $\Omega^{-1}m^{-1}$ at 600 K, by considering the same electrons relaxation time as before. As a consequence, the power factor (Figure 9a) and the figure of merit (Figure 9b) are quite large, especially at 600 K with values of 16.1 $mWm^{-1}s^{-1}$ for PF and hence 16.1 for *ZT*.

In conclusion, the TE properties of $BaRh_2Ge_4S_4Te_2$ are intermediate between those of $BaRh_2Ge_4Se_6$ and $BaRh_2Ge_4Te_6$. More precisely, they are much closer to that of $BaRh_2Ge_4Te_6$ even though the amount of Te is significantly smaller (in at.%), which is a great asset for application purposes. It is then likely that even small additions of Te in the $BaRh_2Ge_4X_6$ (X = S, Se) compounds could lead to much improved TE properties.

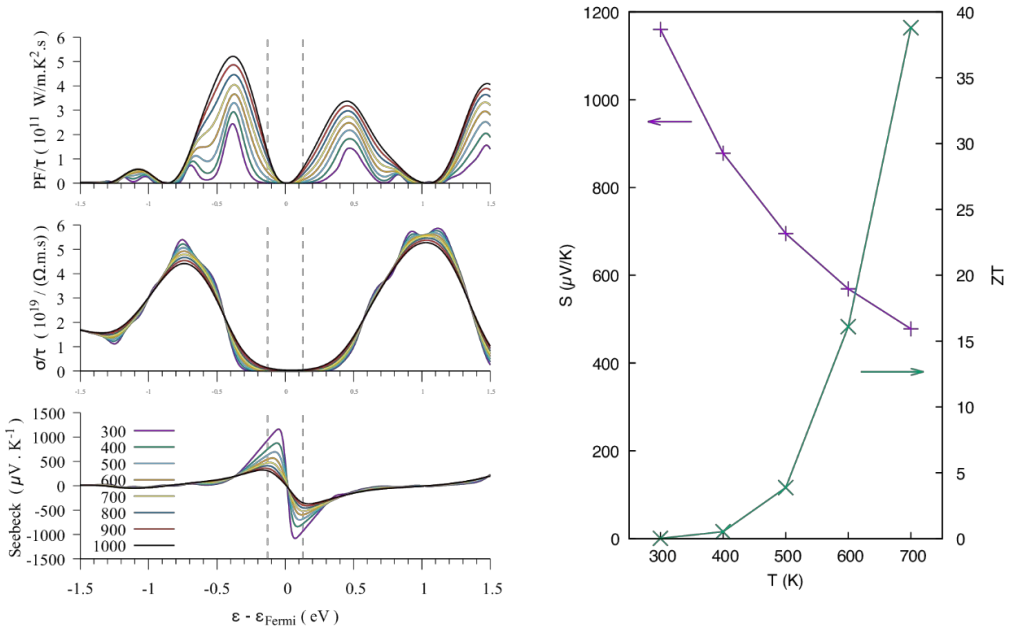

(**a**) (**b**)

Figure 9. Thermoelectric properties of $BaRh_2Ge_4S_4Te_2$. (**a**) Properties plotted w.r.t. Fermi level for temperatures ranging from 300 to 1000 K. Bottom: Seebeck coefficient; middle: electrical conductivity; top: power factor. (**b**) Seebeck coefficient and ZT plotted w.r.t. temperature.

4. Electron Density Topology Analysis

Following our previous works on the chemical bonding analysis for unravelling the structure–property relationships in materials [50,51], we plotted the bond degree [52] H_b/ρ_b with respect to $|V_b|/G_b$, where H stands for the total energy density and the subscript b denotes that these quantities were evaluated at the bond critical points. An analysis of this plot could be performed in frame of the following equation:

$$\frac{H_b}{\rho_b} = \frac{G_b}{\rho_b}\left(1 - \frac{|V_b|}{G_b}\right) \tag{8}$$

which is simply obtained by recasting the expression of the total density energy $H = G + V$ expressed at the BCP. We note that Equation (8) is valid only if the Kirzhnits approximation holds as explained in [50].

The data calculated at the BCPs of the $BaRh_2Ge_4X_6$ and $BaRh_2Ge_4S_4Te_2$ compounds are gathered in Table S1. R_1 and R_2 are the distance from the BCP to the nuclei, and θ is the angle at the BCP formed by the two nuclei and the BCP. The bond characteristics for all the compounds are plotted in Figure 10. We can note that a property of Equation (8) is that the corresponding curve passes through the point (1,0).

A relatively linear relation passing through this point is observed in the region delineated by the boundaries $0.8 \leq |V|/G \leq 1.22$ and $-0.1 \leq H/\rho \leq 0.1$. For all these bonds, the interatomic distance is large (≥3 Å), the electron density Laplacian is positive and small at the BCP (see Figure 11a,b and Table S1) and the total energy density is also positive (Figure 12a,b) or slightly negative (Figure 10). These features are typical of closed shell interactions [20]. The kinetic energy per electron (G/ρ), which is the slope of the line, lies in the range 0.30–0.65 Ry/e, except for the S-S bond in $BaRh_2Ge_4S_4Te_2$ that shows much smaller values (Table S1). The nature of the chemical bond can be refined from the valence shell charge concentration (VSCC) maps (Figure 11). For both Ba-X and X-X (X = S, Se, Te) bonds, the VSCC at the bond critical points show charge depletion, as mentioned above. For the X-X interaction, a large region of charge accumulation is visible at the atom periphery with nearly spherical shape (Figure 11a).

For the Ba-X interaction, the barium atom exhibits large electron density depletion in the outer shells, whereas the chalcogen atom is surrounded by a charge accumulation (Figure 11b). Hence, we can presume that the former interaction is of van der Waals nature, whereas the later one is of ionic type. The ionic character of the Ba-X bond is further confirmed by the calculation of the Bader atomic charge and volume (Table 3); the charge on Ba lies in the range 1.3–1.5e and that of the chalcogenide bonded to Ba varies from –0.31e for Te to –0.99e for S with the general trend $Q(S) < Q(Se) < Q(Te)$. A peculiar S-S interaction in $BaRh_2Ge_4S_4Te_2$ is observed (Figure 10) with a large $|V|/G$ ratio of 2.38, small negative bond degree (–0.08) and very small slope G/ρ of 0.05. In fact, as with the previously described interactions, according to the VSCC (Figure 11c), this interaction presumably corresponds to a dispersive one, in spite of a tiny area of negative total energy density showing up near the BCP (Figure 12c).

The Rh-X bondings of the $BaRh_2Ge_4X_6$ compounds are all located in the region $1.25 \leq |V|/G \leq 1.6$ (Figure 10). For X = S and X = Se, the three bond degree values for each Rh-X interaction roughly lie on a straight line with G/ρ equal to about 0.83 and 0.85, respectively, which is a sign of a similar bonding environment of Rh [50,51] and is corroborated by the distorted octahedron around Rh of the structures in both cases. For Rh-Te, the bond degree values are nearly equal to each other (0.34). Except for one Rh-Te BCP in the $BaRh_2Ge_4S_4Te_2$ compound, the electron density Laplacian values at the BCPs are all positive, which evidences electron depletion at this place. Nevertheless, the bonding is dominated by the potential energy (negative bond degree). The electron density Laplacian and total energy density maps look rather similar (Figures 11d and 12d) and the bonding features of ionic type; for instance, the atomic charge on the sulphur and rhodium atoms are –0.58e and close to zero, respectively, for $BaRh_2Ge_4S_6$ (Table 3). In the particular case of $BaRh_2Ge_4S_4Te_2$ for which one BCP has a negative electron density Laplacian value, the VSCC of both Rh and Te is fairly spherical (Figure 11e). In the basin of Te, the Laplacian map features an extended accumulation of electron density that belongs to Rh and the map of H exhibits a negative energy envelope around the BCP (Figure 12e). From these observations, the Rh-Te bond in $BaRh_2Ge_4S_4Te_2$ can be described as a polar covalent bond, which is supported by the small electronegativity difference between both atoms (χ(Te) = 2.1 and χ(Rh) = 2.28 in Pauling's scale) and the Bader atomic changes (–0.43e for Rh and about zero for Te).

In the region $1.6 \leq |V|/G \leq 2.3$ lie the bonds Rh-Ge and Ge-X in the BD vs. $|V|/G$ map (Figure 10). The Rh-Ge VSCCs (Figure 11e) show a rather spherical shape for both atoms. The BCP is displaced towards the Rh basin, which can be explained by the positive atomic charge borne by Ge (0.78e) and nearly null one of Rh (–0.09e), which agrees with the electronegativity difference (χ(Ge) = 2.01, χ(Rh) = 2.28). Although electron depletion occurs at the BCP ($\nabla^2\rho > 0$), the energy is dominated by the potential energy density ($H < 0$, see Figure 12f). One can note that, as S is replaced by Se and Te, the atomic charge on both the Ge and Rh atoms decreases: 0.78e, 0.62e and 0.41e for Ge in the S, Se and Te-containing compounds, and –0.09e, –0.21e and –0.40e for Rh. In $BaRh_2Ge_4S_4Te_2$, the charge borne by Ge reduces further (0.56e), whereas that of Rh remains the same (–0.43e). These observations allow us to infer that the Rh-Ge bonds are of polar-covalent nature. As for the Ge-X bondings, a negative Laplacian and negative total energy density at the BCP characterize them (e.g., Figures 11g and 12g for Ge-Te in $BaRh_2Ge_4Te_6$). The atomic charges borne by the atoms range from 0.41 to 0.95e and –0.31 to –0.99e for Ge and X (X = S, Se, Te), respectively (Table 3). The more electronegative the chalcogen, the more negative its charge and the more positive that of Ge. Nonetheless, we can infer that the bonding is of polar-covalent nature.

According to Lei et al. [24], for $BaRh_2Ge_4S_6$, assuming the atomic charges +2e, +3e and –2e on Ba, Rh and S, respectively, we obtain the "unusual" charge of +1e on Ge. However, considering the Bader charges on the atoms (Table 3), the picture could be different. Indeed, first, the atomic charge on Rh is close to zero (even slightly negative) and second, the sulphur atoms bear charges that vary from –0.58 to –0.99e. We assume then that the oxidation state of rhodium is zero. As the Bader charge on Ba is large (+1.47e), one can consider that its oxidation state is +II. There are three types of sulphur atoms in the structure, each having multiplicity of 2: S1 bonded to one rhodium and one germanium

atoms, S2 bonded to one barium and three germanium atoms and S3 bonded to four barium and one germanium atoms. Considering the S-Ba bond as an ionic one (see above), S3 should bear a charge of –2e. By contrast, the Rh-S and Ge-S bonds are polar covalent ones; therefore, S1 and S2 could bear a charge of −1e. Accordingly, the charge on germanium would be +2e. This oxidation state agrees well with the large Bader atomic charge found for Ge (+0.78e and +0.95e). To further support this analysis, the $BaRh_4Ge_4$ compound that contains atoms present in our structures except for sulphur was investigated. This compound was synthesized [53] and its chemical and physical properties theoretically investigated [54]. The structure and atomic charges borne by the atoms are presented in Figure S1 and Table S2, respectively. In $BaRh_4Ge_4$, the Rh atom bears a very negative charge of −0.56e, whereas the Ge charge is nearly zero and that of Ba amounts to 1.23e. Hence, as we can see, the Rh atom can bear unusual atomic charge in inorganic solids, in contrast with the situation in inorganic complexes where its oxidation state is often +III.

It is obvious that the $BaRh_2Ge_4X_6$ and $BaRh_2Ge_4S_4Te_2$ structures exhibit various types of bonding: van der Waals, ionic and polar-covalent. As reported in our previous work [51], the large variety of bonding features is particularly beneficial to the thermoelectric properties of compounds, as covalent bonding facilitates electronic conduction, while ionic bonding is favourable to Seebeck effect and van der Waals allows for decreasing the thermal conductivity. Referring to the electronic conduction units (ECU) introduced by Bu et al. [55] one can distinguish different units that act either as a barrier to electron conduction or, on the contrary, as promoters. The Ba-X_{10} units, with their ionic bonding, are prone to favour the Seebeck coefficient, while the $RhGe_{3\times3}$ distorted octahedra, with their polar-covalent bonding, rather promote electron conduction. The Ge-X bonds that link the Ba-X_{10} units to the $RhGe_{3\times3}$ ones, with polar-covalent bonding, fall in the latter category too. In the predicted $BaRh_2Ge_4S_4Te_2$ compound, the bonding picture is essentially the same as that of the $BaRh_2Ge_4X_6$ ones. However, the fact that a small amount of Te substitution in the structure leads to much improved TE properties is probably related to the polar-covalent bonding nature of Te with its neighbours; indeed, the bonding is more covalent than for S and Se, which favours the electron conduction (larger electrical conductivity, see above), especially with respect to sulphur, but still the bonding contains ionicity to some extend that leads to a good Seebeck coefficient. Furthermore, these characteristics of the tellurium bonding with neighbouring atoms can probably be generalized to other Te-containing compounds, hence explaining their, generally good, TE properties.

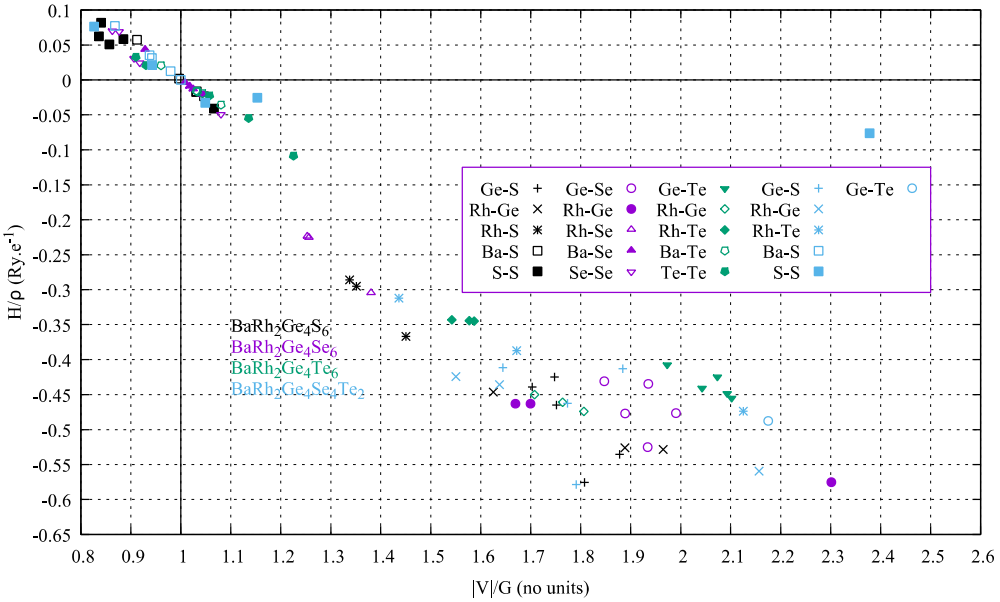

Figure 10. Bond degree vs. $|V|/G$ for the $BaRh_2Ge_4X_6$ (X = S, Se, Te) and $BaRh_2Ge_4S_4Te_2$ compounds.

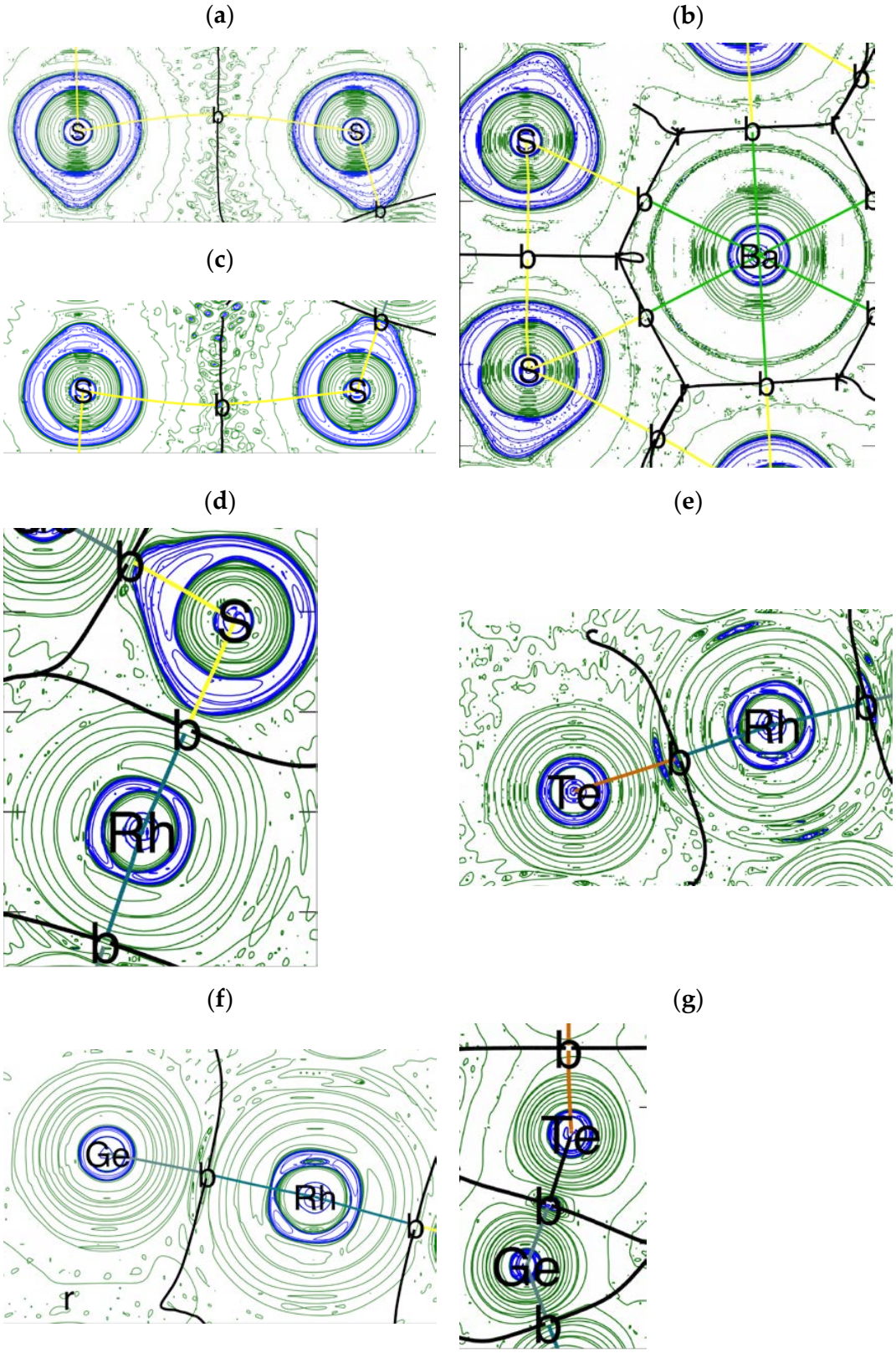

Figure 11. Valence-shell charge concentration (VSCC) of selected pairs of interacting atoms. (**a**) S-S in $BaRh_2Ge_4S_6$; (**b**) Ba-S in $BaRh_2Ge_4S_6$; (**c**) S-S in $BaRh_2Ge_4S_4Te_2$; (**d**) Rh-S in $BaRh_2Ge_4S_6$; (**e**) Te-Rh in $BaRh_2Ge_4S_4Te_2$; (**f**) Rh-Ge in $BaRh_2Ge_4S_6$; (**g**) Ge-Te in $BaRh_2Ge_4Te_6$. Electron density depletion in green; electron density accumulation in blue.

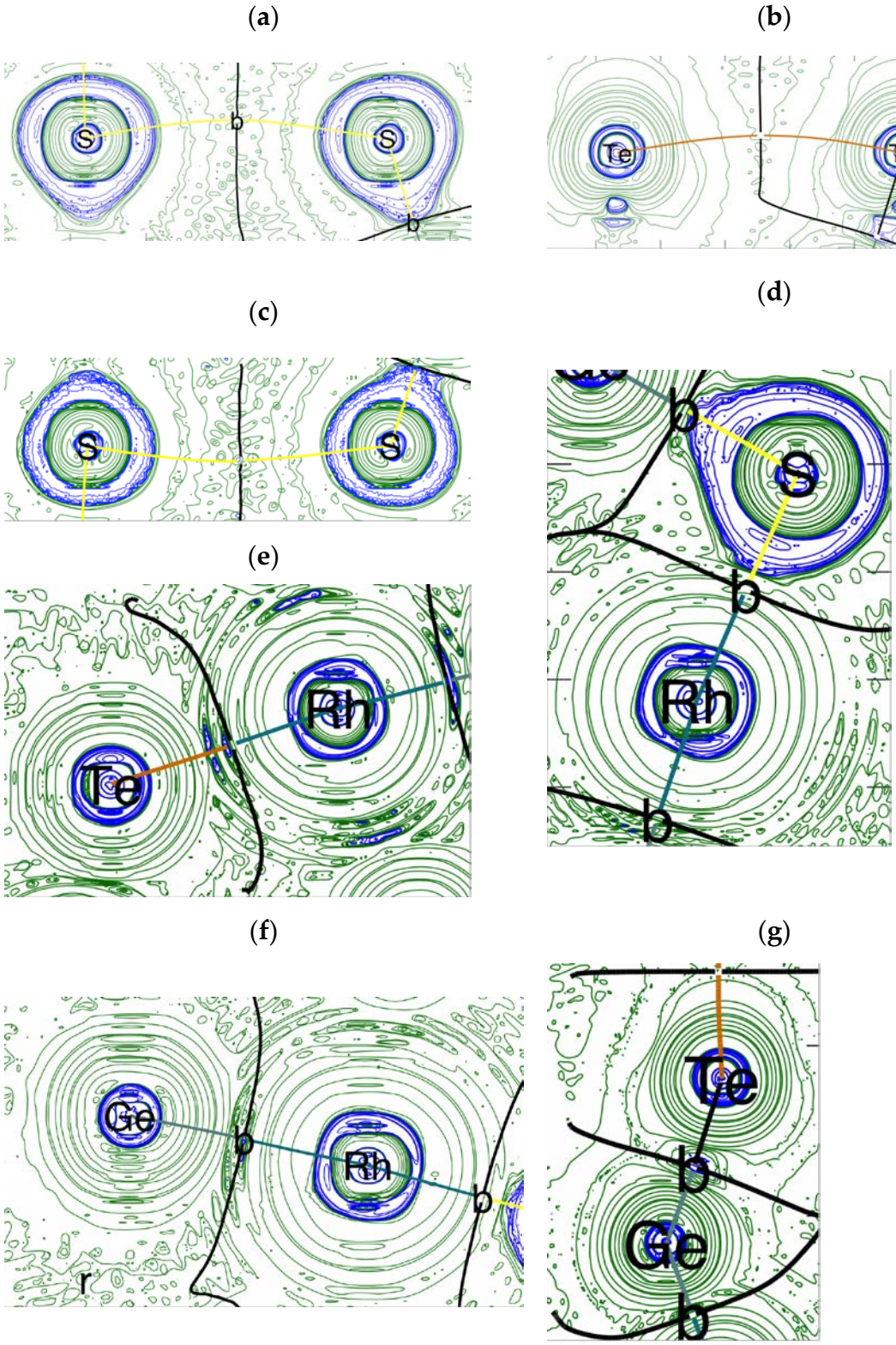

Figure 12. Total energy density (H) map of selected pairs of interacting atoms. (**a**) S-S in $BaRh_2Ge_4S_6$; (**b**) Te-Te in $BaRh_2Ge_4Te_6$; (**c**) S-S in $BaRh_2Ge_4S_4Te_2$; (**d**) Rh-S in $BaRh_2Ge_4S_6$; (**e**) Te-Rh in $BaRh_2Ge_4S_4Te_2$; (**f**) Rh-Ge in $BaRh_2Ge_4S_6$; (**g**) Ge-Te in $BaRh_2Ge_4Te_6$. Positive energy in green; negative energy in blue.

Table 3. Atomic charge (in unit of e) and atomic volume change (in % with respect to the atomic volume obtained from IAM (independent atom model) [56]).

Compound	Atom	Charge	Volume Change
$BaRh_2Ge_4S_6$	Ba	1.47	−8.3
	Rh	−0.09	4.4
	Ge	0.78	−9.4
		0.95	−12.7
	S	−0.58	3.7
		−0.81	7.0
		−0.99	7.7
$BaRh_2Ge_4Se_6$	Ba	1.41	−8.3
	Rh	−0.21	5.2
	Ge	0.62	−8.0
		0.72	−10.1
	Se	−0.36	2.0
		−0.60	4.6
		−0.87	6.7
$BaRh_2Ge_4Te_6$	Ba	1.32	−6.4
	Rh	−0.40	7.1
	Ge	0.41	5.4
		0.40	5.8
	Te	−0.03	−0.8
		−0.31	0.6
		−0.72	5.1
$BaRh_2Ge_4S_4Te_2$	Ba	1.50	−9.6
	Rh	−0.43	7.3
	Ge	0.56	−7.1
		0.93	−13.4
	Te	−0.01	−0.8
	S	−0.82	6.8
		−0.98	9.8

5. Conclusions

The bonding and thermoelectric properties of the $BaRh_2Ge_4X_6$ (X = S, Se and Te) series of compounds were investigated. We found that the compounds are semiconductors and that their gap decreases from sulphur to selenium and to tellurium. The spin–orbit coupling has no impact on the band structures. The highest figure of merit is found for the Te-containing compound as it exhibits large electrical conductivity, due to small band gap, and decent Seebeck effect. The *ZT* equals 1.51 at 300 K. As the $BaRh_2Ge_4Te_6$ compound has not yet been shown to be a stable phase, we investigated the substitution of tellurium for a fraction of sulphur in the $BaRh_2Ge_4S_6$ compound. The corresponding compound is $BaRh_2Ge_4S_4Te_2$. We have shown that this compound leads to a good compromise between good thermoelectric properties offered by the materials and its potential hazard (low content of Te). The topology of the electron density was investigated using Bader's theory of atoms in molecules and crystal. QTAIMAC allowed us to unravel the wide variety of bonding types,

van der Waals, ionic and polar-covalent that prevail in these compounds. This is typified by the graph of the bond degree with respect to the $|V|/G$ ratio at the BCP. From the analysis of the electron density topology, we conclude that this large variety of bonding is responsible for the good thermoelectric properties of the compounds and that the polar-covalent bonds formed by Te with neighbouring atoms could explain the good TE properties of Te-containing materials.

Supplementary Materials: The following are available online at http://www.mdpi.com/1996-1073/13/23/6434/s1, Table S1: Topological properties of the electron density at the bond critical points of the $BaRh_2Ge_4X_6$ (X = S, Se, Te) and $BaRh_2Ge_4S_4Te_2$ compounds. r in e/bohr^3, Dr in e/bohr^5, G and V in Ry/bohr^3, H/r and G/r in Ry/e, R, R_1 and R_2 in Bohr, q in degree. Figure S1: Structure of the $Ba_2Rh_4Ge_4$ compound. The barium atom (big, green balls) is surrounded by six germanium ones (purple), forming an inverted bipyramid (rectangular trapezoprism). The rhodium atom (kaki) is at the centre of a tetrahedron formed by four germanium atoms. Table S2: Atomic charges borne by the Ba, Rh and Ge atoms in the $Ba_2Rh_4Ge_4$ structure.

Author Contributions: Formal analysis, P.B. and M.-C.R.; writing—original draft preparation, P.B. and M.-C.R.; writing—review and editing, P.B. and M.-C.R.; project administration, P.B. and M.-C.R. All authors have read and agreed to the published version of the manuscript.

Funding: This research received no external funding.

Acknowledgments: This work was granted access to the HPC resources of the Centre Informatique National de l'Enseignement Supérieur (CINES), Montpellier, France under allocation A0050806881 made by the Grand Equipement National de Calcul Intensif (GENCI). It was also granted access to the HPC resources of Aix-Marseille Université financed by the project Equip@Meso (ANR-10-EQPX-29-01) of the program "Investissements d'Avenir" supervised by the Agence Nationale de la Recherche.

Conflicts of Interest: The authors declare no conflict of interest.

References

1. Biswas, K.; He, J.; Blum, I.D.; Wu, C.I.; Hogan, T.P.; Seidman, D.N.; Dravid, V.P.; Kanatzidis, M.G. High-performance bulk thermoelectrics with all-scale hierarchical architectures. *Nature* **2012**, *489*, 414–418. [CrossRef]
2. Hsu, K.F.; Loo, S.; Guo, F.; Chen, W.; Dyck, J.S.; Uher, C.; Hogan, T.; Polychroniadis, E.K.; Kanatzidis, M.G. Cubic AgPb(m)SbTe(2+m): Bulk thermoelectric materials with high figure of merit. *Science* **2004**, *303*, 818–821. [CrossRef]
3. Poudeu, P.F.R.; D'Angelo, J.; Downey, A.D.; Short, J.L.; Hogan, T.P.; Kanatzidis, M.G. High thermoelectric figure of merit and nanostructuring in bulk p-type $Na_{1-x}Pb_mSb_yTe_{m+2}$. *Angew. Chem. Int. Ed.* **2006**, *45*, 3835–3839. [CrossRef] [PubMed]
4. Nolas, G.S.; Cohn, J.L.; Slack, G.A.; Schujman, S.B. Semiconducting Ge clathrates: Promising candidates for thermoelectric applications. *Appl. Phys. Lett.* **1998**, *73*, 3133–3144. [CrossRef]
5. Keppens, V.; Mandrus, D.; Sales, B.C.; Chakoumakos, B.C.; Dai, P.; Coldea, R.; Maple, M.B.; Gajewski, D.A.; Freeman, E.J.; Bennington, S. Localized vibrational modes in metallic solids. *Nature* **1998**, *395*, 876–878. [CrossRef]
6. Sales, B.C.; Chakoumakos, B.C.; Mandrus, D. Thermoelectric properties of thallium-filled skutterudites. *Phys. Rev. B* **2000**, *61*, 2475–2481. [CrossRef]
7. Christensen, M.; Abrahamsen, A.B.; Christensen, N.B.; Juranyi, F.; Andersen, N.H.; Lefmann, K.; Andreasson, J.; Bahl, C.R.H.; Iversen, B.B. Avoided crossing of rattler modes in thermoelectric materials. *Nat. Mater.* **2008**, *7*, 811–815. [CrossRef]
8. Zhang, J.; Song, L.; Madsen, G.K.H.; Fischer, K.F.F.; Zhang, W.; Shi, X.; Iversen, B.B. Designing high-performance layered thermoelectric materials through orbital engineering. *Nat. Commun.* **2016**, *7*, 10892. [CrossRef]
9. Heremans, J.P.; Wiendlocha, B.; Chamoire, A.M. Resonant levels in bulk thermoelectric semiconductors. *Energy Environ. Sci.* **2012**, *5*, 5510–5530. [CrossRef]
10. Balout, H.; Boulet, P.; Record, M.C. Electronic and transport properties of Mg_2Si under isotropic strains. *Intermetallics* **2014**, *50*, 8–13. [CrossRef]
11. Balout, H.; Boulet, P.; Record, M.C. Strain-induced electronic band convergence: Effect on the Seebeck coefficient of Mg_2Si for thermoelectric applications. *J. Mol. Mod.* **2017**, *23*, 130. [CrossRef] [PubMed]

12. Pauling, L. The nature of the chemical bond. IV The energy of single bonds and the relative electronegativity of atoms. *J. Am. Chem. Soc.* **1932**, *54*, 3570–3582. [CrossRef]
13. Parr, R.G.; Donnelly, R.A.; Levy, M.; Palke, W.E. Electronegativity: The density functional viewpoint. *J. Chem. Phys.* **1978**, *68*, 3801–3807. [CrossRef]
14. Parr, R.G.; Pearson, R.G. Absolute Hardness: Companion Parameter to Absolute Electronegativity. *J. Am. Chem. Soc.* **1983**, *105*, 7512–7516. [CrossRef]
15. Parr, R.G.; Yang, W. Density Functional Approach to the Frontier-Electron Theory of Chemical Reactivity. *J. Am. Chem. Soc.* **1984**, *106*, 4049–4050. [CrossRef]
16. Pearson, R.G. Recent advances in the concept of hard and soft acids and bases. *J. Chem. Educ.* **1987**, *64*, 561–567. [CrossRef]
17. Chermette, H. Chemical reactivity indexes in density functional theory. *J. Comput. Chem.* **1999**, *20*, 129. [CrossRef]
18. Morell, C.; Grand, A.; Toro-Labbé, A. New Dual Descriptor for Chemical Reactivity. *J. Phys. Chem. A* **2005**, *109*, 205–212. [CrossRef]
19. Bader, R.F.W. *Atoms in Molecules*; Clarendon Press: Oxford, UK, 1990.
20. Gatti, C. Chemical bonding in crystals: New directions. *Z. Kristallogr.* **2005**, *220*, 399–457. [CrossRef]
21. Evangeli, C.; Spiece, J.; Sangtarash, S.; Molina-Mendoza, A.J.; Mucientes, M.; Mueller, T.; Lambert, C.; Sadeghi, H.; Kolosov, O. Nanoscale Thermal Transport in 2D Nanostructures from Cryogenic to Room Temperature. *Adv. Electron. Mater.* **2019**, *5*, 1900331. [CrossRef]
22. Oh, J.; Kim, Y.; Chung, S.; Kim, H.; Son, J.G. Fabrication of a MoS_2/Graphene Nanoribbon Heterojunction Network for Improved Thermoelectric Properties. *Adv. Mater. Interf.* **2019**, *6*, 1901333. [CrossRef]
23. Uematsu, Y.; Terada, T.; Sato, K.; Ishibe, T.; Nakamura, Y. Low thermal conductivity in single crystalline epitaxial germanane films. *Appl. Phys. Express* **2020**, *13*, 55503. [CrossRef]
24. Lei, H.; Yamaura, J.I.; Guo, J.; Qi, Y.; Toda, Y.; Hosono, H. Layered Compounds $BaM_2Ge_4Ch_6$ (M = Rh, Ir and Ch = S, Se) with Pyrite-Type Building Blocks and Ge–Ch Heteromolecule-Like Anions. *Inorg. Chem.* **2014**, *53*, 5684–5691. [CrossRef] [PubMed]
25. Bader, R.F.W.; Essén, H. The characterization of atomic interactions. *J. Chem. Phys.* **1984**, *80*, 1943–1960. [CrossRef]
26. Bader, R.F.W. Bond Paths Are Not Chemical Bonds. *J. Phys. Chem. A* **2009**, *113*, 10391–10396. [CrossRef]
27. Silvi, B.; Savin, A. Classification of chemical bonds based on topological analysis of electron localization functions. *Nature* **1994**, *371*, 683–686. [CrossRef]
28. Silvi, B.; Gatti, C. Direct Space Representation of the Metallic Bond. *J. Chem. Phys. A* **2000**, *104*, 947–953. [CrossRef]
29. Cremer, D.; Kraka, E. A description of the chemical bond in terms of local properties of electron density and energy. *Croat. Chem. Acta* **1984**, *57*, 1259–1281.
30. Kirzhnits, D.A. Quantum Corrections to the Thomas-Fermi Equation. *Sov. Phys. JETP* **1957**, *5*, 64.
31. Hodges, C.H. Quantum Corrections to the Thomas–Fermi Approximation—The Kirzhnits Method. *Can. J. Phys.* **1973**, *51*, 1428–1437. [CrossRef]
32. Abramov, Y.A. Secondary Interactions and Bond Critical Points in Ionic Crystals. *Acta Cryst. Sect. A Found. Cryst.* **1997**, *53*, 264–272. [CrossRef]
33. Hohenberg, P.; Kohn, W. Inhomogeneous Electron Gas. *Phys. Rev.* **1964**, *136*, B864–B871. [CrossRef]
34. Kohn, W.; Sham, L.J. Self-Consistent Equations Including Exchange and Correlation Effects. *Phys. Rev.* **1965**, *140*, A1133–A1138. [CrossRef]
35. Perdew, J.; Burke, K.; Ernzerhof, M. Generalized Gradient Approximation Made Simple. *Phys. Rev. Lett.* **1996**, *77*, 3865–3868. [CrossRef]
36. Blöchl, P.E. Projector augmented-wave method. *Phys. Rev. B* **1994**, *50*, 17953–17979. [CrossRef]
37. Perdew, J.P.; Ruzsinszky, A.; Csonka, G.I.; Vydrov, O.A.; Scuseria, G.E.; Constantin, L.A.; Zhou, X.; Burke, K. Restoring the density-gradient expansion for exchange in solids and surfaces. *Phys. Rev. Lett.* **2008**, *100*, 136406. [CrossRef]
38. Medasani, B.; Haranczyk, M.; Canning, A.; Asta, M. Vacancy formation energies in metals: A comparison of MetaGGA with LDA and GGA exchange-correlation functionnals. *Comput. Mater. Sci.* **2015**, *101*, 96–107. [CrossRef]

39. Shang, S.; Wang, Y.; Guan, P.; Wang, W.Y.; Fang, H.; Anderson, T.; Liu, Z.K. Insight into structural, elastic, phonon, and thermodynamic properties of α-sulfur and energy-related sulfides: A comprehensive first-principles study. *J. Mater. Chem. A* **2015**, *3*, 8002–8014. [CrossRef]
40. Tran, F.; Koller, D.; Blaha, P. Application of screened hybrid functionals to the bulk transition metals Rh, Pd, and Pt. *Phys. Rev. B* **2012**, *86*, 134406. [CrossRef]
41. Giannozzi, P.; Baroni, S.; Bonini, N.J. QUANTUM ESPRESSO: A modular and open-source software project for quantum simulations of materials. *J. Phys. Condens. Matter* **2009**, *21*, 395502. [CrossRef]
42. Giannozzi, P.; Andreussi, O.; Brumme, T. Advanced capabilities for materials modelling with Quantum ESPRESSO. *J. Phys. Condens. Matter* **2017**, *29*, 465901. [CrossRef] [PubMed]
43. Madsen, G.K.H.; Singh, D.J. BoltzTraP. A code for calculating band-structure dependent quantities. *Comput. Phys. Commun.* **2006**, *175*, 67–71. [CrossRef]
44. Otero-de-la-Roza, A.; Blanco, M.A.; Martín Pendás, A.; Luaña, V. Critic: A new program for the topological analysis of solid-state electron densities. *Comput. Phys. Commun.* **2009**, *180*, 157–166. [CrossRef]
45. Otero-de-la-Roza, A.; Johnson, E.R.; Luaña, V. Critic2: A program for real-space analysis of quantum chemical interactions in solids. *Comput. Phys. Commun.* **2014**, *185*, 1007–1018. [CrossRef]
46. Momma, K.; Izumi, F. *VESTA 3* for three-dimensional visualization of crystal, volumetric and morphology data. *J. Appl. Cryst.* **2011**, *44*, 1272–1276. [CrossRef]
47. Available online: http://www.gnuplot.info (accessed on 3 December 2020).
48. Lin, S.; Li, W.; Bu, Z.; Gao, B.; Li, J.; Pei, Y. Thermoelectric properties of Ag9GaS6 with ultralow lattice thermal conductivity. *Mater. Today Phys.* **2018**, *6*, 60–67. [CrossRef]
49. Li, Y.; Li, Z.; Zhang, C.; Yang, D.; Liu, T.; Yan, Y.; Liu, W.; Tan, G.; Su, X.; Uher, C.; et al. Ultralow thermal conductivity of $BaAg_2SnSe_4$ and the effect of doping by Ga and In. *Mater. Today Phys.* **2019**, *9*, 100098. [CrossRef]
50. Yang, H.; Boulet, P.; Record, M.C. A rapid method for analyzing the chemical bond from energy densities calculations at the bond critical point. *Comput. Theor. Chem.* **2020**, *1178*, 112784. [CrossRef]
51. Yang, H.; Boulet, P.; Record, M.C. New insight into the structure-property relationships from chemical bonding analysis: Application to thermoelectric materials. *J. Solid State Mater.* **2020**, *286*, 121266. [CrossRef]
52. Espinosa, E.; Alkorta, I.; Elguero, J.; Molins, E. From weak to strong interactions: A comprehensive analysis of the topological and energetic properties of the electron density distribution involving X–H···F–Y systems. *J. Chem. Phys.* **2002**, *117*, 5529–5542. [CrossRef]
53. Gonzalez, J.; Kessens, R.; Schuster, H.U. Darstellung und Kristallstruktur neuer AM_2X_2-Verbindungen in den Systemen Erdalkalimetall-Platinmetall-Germanium. *Z. Anorg. Allg. Chem.* **1993**, *619*, 13–16. [CrossRef]
54. Salma, M.U.; Rahman, M.A. Physical properties of $ThCr_2Si_2$-type Rh-based compounds ARh_2Ge_2 (A = Ca, Sr, Y and Ba): DFT based first-principles investigation. *Int. J. Mod. Phys. B* **2018**, *32*, 1850357. [CrossRef]
55. Bu, K.; Huang, J.; Luo, M.; Guan, M.; Zheng, C.; Pan, J.; Zhang, X.; Wang, S.; Zhao, W.; Shi, X.; et al. Observation of High Seebeck Coefficient and Low Thermal Conductivity in [SrO]-Intercalated $CuSbSe_2$ Compound. *Chem. Mater.* **2018**, *30*, 5539–5543. [CrossRef]
56. Coppens, P. *X-Ray Charge Densities and Chemical Bonding, IUCr Texts on Crystallography*; Oxford University Press: Oxford, UK, 1997; Volume 4.